HARPS-N Solar RVs Are Dominated by Large, Bright Magnetic Regions

T. W. Milbourne[1,2] ᴵᴰ, R. D. Haywood[2,16] ᴵᴰ, D. F. Phillips[2] ᴵᴰ, S. H. Saar[2], H. M. Cegla[3,17] ᴵᴰ, A. C. Cameron[4] ᴵᴰ, J. Costes[5],
X. Dumusque[3] ᴵᴰ, N. Langellier[1,2], D. W. Latham[2] ᴵᴰ, J. Maldonado[6] ᴵᴰ, L. Malavolta[7,8] ᴵᴰ, A. Mortier[4,9] ᴵᴰ, M. L. Palumbo III[2,10],
S. Thompson[9], C. A. Watson[5], F. Bouchy[3] ᴵᴰ, N. Buchschacher[3] ᴵᴰ, M. Cecconi[11], D. Charbonneau[2] ᴵᴰ, R. Cosentino[11],
A. Ghedina[11] ᴵᴰ, A. G. Glenday[2] ᴵᴰ, M. Gonzalez[11], C-H. Li[2], M. Lodi[11] ᴵᴰ, M. López-Morales[2] ᴵᴰ, C. Lovis[3], M. Mayor[3],
G. Micela[6] ᴵᴰ, E. Molinari[11,12] ᴵᴰ, F. Pepe[3], G. Piotto[7,8] ᴵᴰ, K. Rice[13,14] ᴵᴰ, D. Sasselov[2], D. Ségransan[3], A. Sozzetti[15] ᴵᴰ,
A. Szentgyorgyi[2], S. Udry[3], and R. L. Walsworth[1,2]
[1] Department of Physics, Harvard University, 17 Oxford Street, Cambridge, MA 02138, USA
[2] Harvard-Smithsonian Center for Astrophysics, Cambridge, MA 02138, USA
[3] Observatoire Astronomique de l'Universite de Génève, 51 Chemin des Maillettes, 1290 Sauverny, Switzerland
[4] Centre for Exoplanet Science, SUPA, School of Physics and Astronomy, University of St Andrews, St Andrews KY16 9SS, UK
[5] Astrophysics Research Centre, School of Mathematics and Physics, Queen's University Belfast, Belfast, BT7 1NN, UK
[6] INAF-Osservatorio Astronomico di Palermo, Piazza del Parlamento 1, I-90134 Palermo, Italy
[7] INAF-Osservatorio Astronomico di Padova, Vicolo dell'Osservatorio 5, I-35122 Padova, Italy
[8] Dipartimento di Fisica e Astronomia "Galileo Galilei," Università di Padova, Vicolo dell'Osservatorio 3, I-35122 Padova, Italy
[9] Astrophysics Group, Cavendish Laboratory, J.J. Thomson Avenue, Cambridge CB3 0HE, UK
[10] Department of Astronomy & Astrophysics, The Pennsylvania State University, University Park, PA 16802, USA
[11] INAF-Fundacion Galileo Galilei, Rambla Jose Ana Fernandez Perez 7, E-38712 Brena Baja, Spain
[12] INAF-Osservatorio Astronomico di Cagliari, Via della Scienza 5, I-09047 Selargius CA, Italy
[13] SUPA, Institute for Astronomy, Royal Observatory, University of Edinburgh, Blackford Hill, Edinburgh EH93HJ, UK
[14] Centre for Exoplanet Science, University of Edinburgh, Edinburgh, UK
[15] INAF-Osservatorio Astrofisico di Torino, via Osservatorio 20, I-10025 Pino Torinese, Italy

Abstract

State-of-the-art radial-velocity (RV) exoplanet searches are currently limited by RV signals arising from stellar magnetic activity. We analyze solar observations acquired over a 3 yr period during the decline of Carrington Cycle 24 to test models of RV variation of Sun-like stars. A purpose-built solar telescope at the High Accuracy Radial-velocity Planet Searcher for the Northern hemisphere (HARPS-N) provides disk-integrated solar spectra, from which we extract RVs and $\log R'_{\rm HK}$. The *Solar Dynamics Observatory* (*SDO*) provides disk-resolved images of magnetic activity. The Solar Radiation and Climate Experiment (SORCE) provides near-continuous solar photometry, analogous to a *Kepler* light curve. We verify that the SORCE photometry and HARPS-N $\log R'_{\rm HK}$ correlate strongly with the *SDO*-derived magnetic filling factor, while the HARPS-N RV variations do not. To explain this discrepancy, we test existing models of RV variations. We estimate the contributions of the suppression of convective blueshift and the rotational imbalance due to brightness inhomogeneities to the observed HARPS-N RVs. We investigate the time variation of these contributions over several rotation periods, and how these contributions depend on the area of active regions. We find that magnetic active regions smaller than $60\,{\rm Mm}^2$ do not significantly suppress convective blueshift. Our area-dependent model reduces the amplitude of activity-induced RV variations by a factor of two. The present study highlights the need to identify a proxy that correlates specifically with large, bright magnetic regions on the surfaces of exoplanet-hosting stars.

Key words: planets and satellites: detection – Sun: activity – Sun: faculae, plages – Sun: granulation – sunspots – techniques: radial velocities

Supporting material: machine-readable table

1. Introduction

The radial-velocity (RV) method is a powerful tool for exoplanet detection and mass estimation (Mayor & Queloz 1995; Fischer et al. 2016). When used in conjunction with transit measurements, as performed by *CoRoT*, *Kepler*, *K2*, and *TESS* (Auvergne et al. 2009; Borucki et al. 2010; Howell et al. 2014; Ricker et al. 2014), the RV method allows for determinations of planetary densities, relevant to studies of the internal structure of detected planets (Zeng & Sasselov 2013). The reflex RV amplitude induced by an Earth-mass planet in the habitable zone of a Sun-like star is about

$10\,{\rm cm\,s}^{-1}$, the target sensitivity of next-generation spectrographs (Pepe et al. 2010). However, RV measurements are currently dominated by the effects of stellar activity. In particular, acoustic oscillations, granulation and supergranulation due to surface magneto-convection, and other stellar activity processes contribute RV signals exceeding $1\,{\rm m\,s}^{-1}$, as discussed by Saar & Donahue (1997), Schrijver & Zwaan (2000), Meunier et al. (2010a, 2015), and Dumusque et al. (2011). These activity processes must be understood to successfully interpret current observations.

Stellar activity processes act on distinct timescales. Over periods of a few minutes, stellar p-modes (i.e., the propagation of acoustic vibrations) are dominant (Broomhall et al. 2009). The upward and downward motion of convecting plasma also

---

contributes to the overall RV signal; these granulation processes (including supergranulation and mesogranulation) are dominant over periods between hours and a few days (Palle et al. 1995; Del Moro 2004; Kjeldsen et al. 2005). Contributions from magnetic features, such as dark sunspots, bright photospheric plage (i.e., the magnetically laced photosphere under chromospheric plage), and photospheric network, dominate on timescales longer than a rotation period (Meunier et al. 2010a; Haywood et al. 2016). Since exoplanet surveys often target low-activity stars, the behavior of stars near activity minimum must be considered to ensure accurate RV detections of low-mass exoplanets.

The close proximity of the Sun makes it an ideal test case for studying different stellar signals and correlating with RV measurements. Numerous ground and space-based instruments, such as Global Oscillations Network Group (Harvey et al. 1988), the SOlar Radiation and Climate Experiment (SORCE, Rottman 2005), and the *Solar Dynamics Observatory* (*SDO*, Pesnell et al. 2012), perform detailed observations of the Sun's surface. In parallel with these instruments, a custom-built solar telescope installed at the Telescopio Nazionale Galileo (TNG) on La Palma makes disk-integrated, spectroscopic measurements of the Sun as a star using the state-of-the-art High Radial-velocity Planet Searcher for the Northern Hemisphere (HARPS-N) spectrograph (Dumusque et al. 2015; Phillips et al. 2016). This allows us to observe the Sun as we would any other star in high-precision RV exoplanet surveys. By comparing this rich data set with solar photometry and disk-resolved images, we investigate the contributions of different activity processes to RV measurements and how these contributions vary over different timescales.

Previously, Meunier et al. (2010b) reconstructed the solar RV using images from the Michelson Doppler Imager (MDI) onboard the *Solar and Heliospheric Observatory*. They also investigated how the convective RV shift scales with active region area. In another work, the authors investigate the relative contributions of large versus small active regions to the solar RV (Meunier et al. 2010a). Haywood et al. (2016) used data from the Helioseismic and Magnetic Imager (HMI, Schou et al. 2012) onboard *SDO* to reconstruct the magnetically driven solar RVs, and compared these to HARPS RVs derived from sunlight reflected off the asteroid Vesta. Both these works, however, suffer from practical limitations: Meunier et al. (2010b) were limited by the spatial resolution of MDI, and were unable to measure the impact of small active regions on the activity-driven RV. While Haywood et al. (2016) used higher-resolution HMI images in their work, their observations of Vesta only spanned 70 days, approximately 2.5 synodic solar rotation periods. In order to fully characterize the effects of magnetic activity on the solar RVs, we need to understand the contributions of large and small active regions, and how these contributions evolve over the course of many rotation periods.

In this work, we use contemporaneous disk-averaged solar telescope spectra, HMI solar images, and SORCE Total Irradiance Monitor (TIM) measurements of the Total Solar Irradiance (TSI; Kopp & Lawrence 2005; Kopp et al. 2005) taken between 2015 July and 2017 September, near the end of Solar Cycle 24, to estimate how the RV contributions from convective and photometric solar magnetic activity vary over several solar rotation periods, approaching solar minimum (late 2018/early 2019). We also investigate how these contributions vary with the size of the active regions producing these RV perturbations.

2. Observations

2.1. Solar Telescope at HARPS-N

The HARPS-N spectrograph at the TNG is a cross-dispersed echelle spectrograph spanning the visible range (Cosentino et al. 2012). During the day, a custom-built solar telescope connected to HARPS-N provides a near-continuous stream of disk-integrated solar spectra (Dumusque et al. 2015; Phillips et al. 2016). This instrument, in operation since 2015, works in combination with the HARPS-N spectrograph to observe the Sun as a star, giving unprecedented temporal coverage (about one exposure every 5 minutes, with a typical daily coverage of 6 hr) of the solar spectrum with resolving power $R = 115,000$ and optical bandwidth spanning 383–690 nm. The solar telescope has a $3''$ lens that feeds an integrating sphere, which scrambles all angular information and converts solar images into the equivalent of a point source. Systematic laboratory and on-sky tests show the solar telescope captures the full disk of the Sun with RV precision below 10 cm s^{-1} as compared to independent *SDO*/HMI images, well below the 40 cm s^{-1} per exposure precision of HARPS-N itself (Cosentino et al. 2014; Phillips et al. 2016).

We acquire 5 minute solar exposures to average over solar acoustic oscillations (*p*-modes) and achieve RV precision of approximately 40 cm s^{-1}. This temporal coverage allows us to investigate solar activity on timescales between minutes and years, as demonstrated in Phillips et al. (2016). To reduce the effects of solar oscillations, granulation, and other processes with variability timescales less than 24 hr, we take daily averages of the solar RVs. The changes in these daily averaged RVs are therefore dominated by stellar activity effects (Meunier et al. 2010a; Dumusque et al. 2015).

Solar RVs are derived from the measured spectra using the HARPS-N Data Reduction System (DRS) (Baranne et al. 1996; Sosnowska et al. 2012). The contributions of planetary reflex motion to the solar RVs are removed using JPL Horizons ephemerides to determine the Sun-TNG relative velocity (Giorgini et al. 1996). The effects of differential atmospheric extinction are removed from the RVs by calculating the intensity-weighted mean rotational velocity across the solar disk, accounting for the extinction gradient across the disk and the inclination of the solar rotation axis to the local vertical, as described in Collier Cameron et al. (2019). Exposures contaminated by clouds are identified using the HARPS-N exposure meter and are removed from the final data set. If any of the 1 s sampled exposure meter measurements are below a certain threshold, the corresponding exposure is rejected. The remaining "RV residuals" are predominantly the result of solar variability (i.e., if the Sun were a uniform, homogeneous disk, they would be consistent with zero and limited to statistical noise and residual spectrograph systematic variations). These residuals have an rms amplitude of 1.6 m s^{-1}, comparable to those observed on stars of similar activity levels (Isaacson & Fischer 2010). Additionally, we extract the calcium S-index, a known correlate of magnetic activity and the derivative R'_{HK} (Vaughan et al. 1978; Noyes et al. 1984), from the Ca II H&K lines in the solar spectra. The resulting values of the HARPS-N RVs and log R'_{HK} are shown in the top two panels of Figure 1.
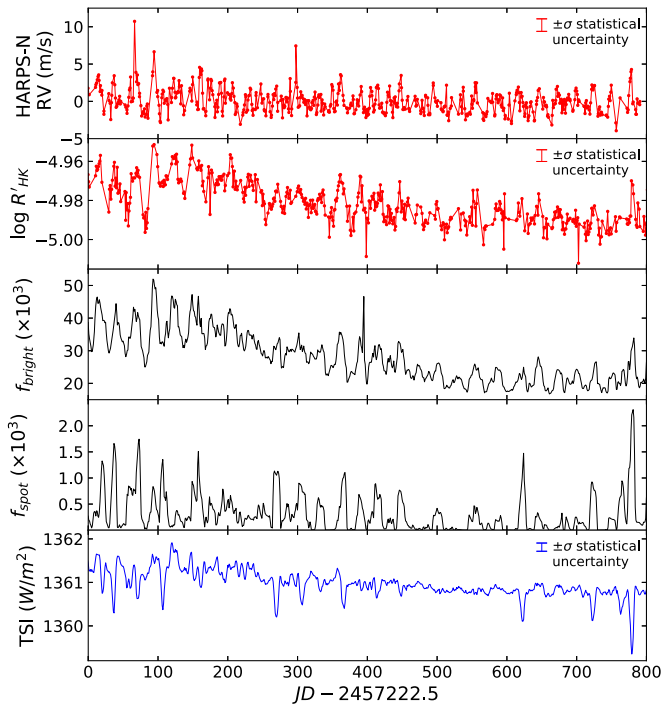
Figure 1. Solar measures used in this work. From top to bottom: solar telescope/HARPS-N RV after subtracting the effects due to all planets using the JPL *Horizons* System (measured relative to the averaged HARPS-N solar RV) and log $R'_{\rm HK}$ (red), *SDO*/HMI bright (plage and network) and dark (spot) filling factors (black), and SORCE/TIM TSI (blue). A noticeable decrease in solar activity beginning around Day 200 is visible in all of the displayed activity indicators but not in the HARPS-N RVs. However, we do note an apparent decrease in the RV scatter at this time. Dips in the TSI are coincident with peaks in the spot filling factor. Observations are taken between 2015 July through 2017 September, with solar minimum expected in late 2018/early 2019. For the solar telescope/HARPS-N and SORCE/TIM derived quantities, we plot a representative $\pm\sigma$ statistical error bar. Since the *SDO*/HMI-derived quantities are determined by averaging over $\sim10^6$ CCD pixels, the associated statistical errors are vanishingly small. We therefore omit error bars for those quantities.

2.2. SDO/HMI

HMI onboard *SDO* captures full-disk images of the Sun with near single-granule resolution (Pesnell et al. 2012; Schou et al. 2012). HMI determines the continuum intensity, line depth, line width, Doppler velocity, and magnetic flux at each point along the solar disk by measuring six wavelengths around the 6173.3 Å neutral iron (Fe I) line in two polarization states (Couvidat et al. 2016).

Using thresholding algorithms pioneered by Fligge et al. (2000) and subsequently used for solar RV modeling by Meunier et al. (2010b) and Haywood et al. (2016), we identify active regions along the solar disk and calculate the magnetic filling factor, $f_{\rm total}$ (see Figure 1), the percentage of the solar disk covered by magnetic activity. We use the same intensity thresholds determined by Yeo et al. (2013) and employed by Haywood et al. (2016) to distinguish between dark regions (sunspots) and bright regions (plage and network), allowing us to calculate filling factors for each type of magnetic feature ($f_{\rm bright}$ and $f_{\rm spot}$, respectively). By combining the intensity and magnetic flux information with the Doppler velocities, we estimate the contributions of magnetic activity to solar RVs.

In this work, we consider the 720 s exposure line-of-sight measurements of the continuum intensity, magnetic field, and Doppler velocity.[18] We use six images each day, sampled evenly over the 2.5 yr operational period of the solar telescope at HARPS-N. Note that all HMI observables have a strong 24 hr modulation related to an imperfect removal of the *SDO* spacecraft's orbit (Couvidat et al. 2016); to mitigate the effects of these and other systematics (Löhner-Böttcher & Schlichenmaier 2013; Reiners et al. 2016; Hoeksema et al. 2018), we therefore reference all derived RVs to the quiet-Sun velocity and take daily averages of the derived filling factors and activity-driven RVs (Meunier et al. 2010b; Haywood et al. 2016). (See Section 4 and Appendix A for further discussion of these calculations.)

2.3. SORCE/TIM

TIM on board SORCE measures the TSI using a set of four Electrical Substitution Radiometers, providing a near-continuous stream of solar photometry analogous to *Kepler* data (Kopp et al. 2005) for the Sun.[19] On timescales between days and months, changes in the TSI are related to the movement of bright and dark active regions across the solar surface (as shown in Figure 1). The TSI therefore functions as a purely photometric measure of the solar activity. While the solar telescope at HARPS-N is equipped with an exposure meter, variable atmospheric transparency, the aging of telescope components, and the lack of a reference source makes ground-based photometry impractical. The space-based SORCE/TIM is therefore a valuable tool in the study of solar activity, allowing us to compare our disk-integrated and disk-resolved data products with simultaneous photometry.

3. Comparing Measurements of Solar Magnetic Activity

The solar telescope, *SDO*/HMI, and SORCE/TIM each provide a unique lens for analyzing solar activity. Using the broadband, spectroscopic information derived from the solar telescope/HARPS-N, we extract the solar RVs, Mt. Wilson S-index, and the derivative index log $R'_{\rm HK}$ (see below for a further discussion of these activity indicators). *SDO*/HMI directly images active regions on the solar disk, allowing us to identify them as sunspots or plage and network. SORCE/TIM measurements of the TSI provide a photometric measurement of solar activity.

Comparing the time series of each activity indicator, shown in Figure 1, we see qualitative agreement between the data products of each instrument. The HARPS-N-derived log $R'_{\rm HK}$, the *SDO*/HMI bright region filling factor (plage and network), the peak amplitudes of the *SDO*/HMI spot filling factor, and the SORCE/TIM TSI all show the same downward trend as the Sun approaches solar minimum. Furthermore, peaks in the spot filling factor are coincident with sharp dips in the SORCE/TIM TSI. In this section, we make quantitative comparisons between these independent measurements of solar activity and demonstrate the instruments provide a consistent picture of solar magnetic processes.

---

[18] Publicly available at http://jsoc.stanford.edu/.
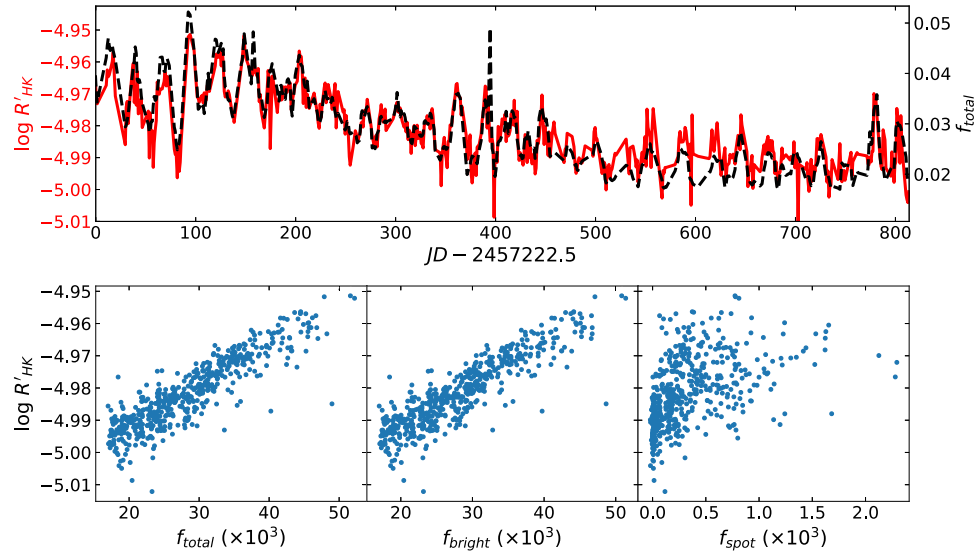[19] Publicly available at http://lasp.colorado.edu/home/sorce/data/tsi-data/.

Figure 2. Top: spectrally derived $\log R'_{HK}$ (black dotted line) and *SDO*/HMI-calculated total magnetic filling factor (red solid line), plotted as a function of time. A strong correlation between the two quantities is clearly visible in the time series. Both indicators demonstrate oscillations at the synodic solar rotation period (28 days). Bottom: correlation plots between $\log R'_{HK}$ and the total filling factor (left), the network and plage filling factor (center), and the spot filling factor (right). We see that the correlation between between the filling factor and $\log R'_{HK}$ is driven by the bright regions: the Sun is a plage-dominated star entering activity minimum, resulting in a factor of $\sim 10^2$ fewer sunspots, and a much weaker correlation with the spot filling factor. This relationship is captured by the Spearman correlation coefficients for each filling factor and $\log R'_{HK}$: the correlation coefficient between the overall filling factor and $\log R'_{HK}$ is 0.8836, the correlation coefficient between the plage/network filling factor and $\log R'_{HK}$ is 0.8833, and the correlation coefficient between the spot filling factor and $\log R'_{HK}$ is 0.590.

3.1. Comparison of SDO/HMI with Solar Telescope/HARPS-N

Magnetic heating of the solar chromosphere results in enhanced emission reversals in the cores of the Ca II H&K lines (Linsky & Avrett 1970). The observed correlation between these emission reversals and sunspot number, as described in Wilson (1968), led to the development of the Mt. Wilson S-index and the color-corrected $\log R'_{HK}$, as defined in Vaughan et al. (1978). Given the correlations between chromospheric plage and the photospheric spots and faculae, we expect a high degree of correlation between $\log R'_{HK}$ and the magnetic filling factors as well (Shapiro et al. 2014).

The *SDO*/HMI-derived magnetic filling factor and spectroscopic measurements of $\log R'_{HK}$ are highly correlated, with a Spearman correlation coefficient of 0.8836. (Figure 2). Dividing the total magnetic filling factor into a bright (plage and network) and dark (spot) contributions also shows the expected behavior; the plage and network, which dominate the total activity, are strongly correlated with $\log R'_{HK}$. The spots, however, cover a much smaller portion of the solar surface ($f_{bright}/f_{spot} > 80$) and exhibit a much weaker correlation with $\log R'_{HK}$.

3.2. Comparison of SDO/HMI with SORCE/TIM TSI

The presence of bright (plage and network) and dark (sunspots) features on the solar surface causes the TSI to fluctuate in response to magnetic activity. This is readily apparent in Figure 1: spikes in the spot filling factor derived from *SDO*/HMI are accompanied by corresponding decreases in the SORCE/TIM TSI and the long-term decrease in the plage and network filling factor are correlated with the long-term decrease of the TSI.

The different brightnesses of these features arise because bright plage and network regions are hotter than the quiet Sun, and that spots are colder. We therefore define ΔT_{bright} and ΔT_{spot}, the brightness temperature contrasts of these two

features. Following Meunier et al. (2010a), we use the *SDO*/HMI-derived plage and spot filling factors to reproduce the measured TSI:

$$\begin{aligned}
\mathrm{TSI} = \mathcal{A}\sigma\,[&(1 - a_{spot}f_{spot} - a_{bright}f_{bright})T_{quiet}^4 \\
&+ a_{spot}f_{spot}(T_{quiet} + \Delta T_{spot})^4 \\
&+ a_{bright}f_{bright}(T_{quiet} + \Delta T_{bright})^4],
\end{aligned} \tag{1}$$

where σ is the Stefan–Boltzmann constant, $\mathcal{A} = (R_\odot/1\ \mathrm{au})^2$ is a geometrical constant relating the energy emitted at the solar surface to the energy received at Earth, T_{quiet} is the quiet-Sun temperature, and f_{spot} and f_{bright} are the HMI spot and plage/network filling factors.

Additionally, a_{bright} and a_{spot} are scaling factors, used to account for systematic differences in the calculation of filling factors. The values of the bright and spot filling factors depend strongly the choice of magnetic flux and intensity thresholds used to differentiate spots, plage, and quiet Sun, as well as the wavelength(s) used to observe these features. Variations in these parameters mean that established sunspot data sets may differ by over 50% (Meunier et al. 2010a). Including these scaling factors in our model allows us to account for these definition-dependent factors and to compare the brightness temperature contrasts of each feature to literature values. Since these scaling factors are constant, multiplicative values, they do not affect correlations between the filling factors and the other activity measurements.

A wide range of spot and plage/network temperature contrasts are given in the literature. From Meunier et al. (2010a), we infer that $-649\ \mathrm{K} < \Delta T_{spot} < -450\ \mathrm{K}$ and $38\ \mathrm{K} < \Delta T_{bright} < 55\ \mathrm{K}$. Note that the apparent temperature of plage varies with position on the solar disk: Since the disk-averaged *SDO*/HMI plage filling factor contains no spatial information, we take ΔT_{bright} to be the average brightness temperature contrast of solar plage. In our analysis, we assume
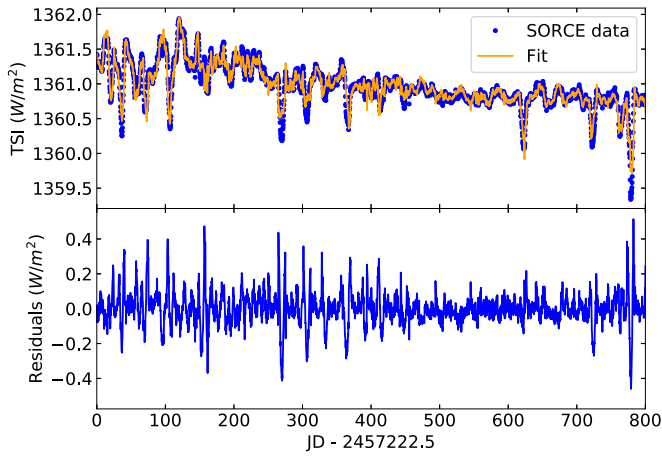
Figure 3. Top: SORCE/TIM measurements of TSI (blue circles), with reconstructed TSI from *SDO*/HMI filling factors (orange line). Bottom: fit residuals. The residuals shown are consistent with the typical SORCE/TIM uncertainty per data point, 0.48 W m^{-2}. Note that the correlation between the TSI and the convective magnetic shift (see Section 4.1) implies an RV scaling with TSI of 3.3 (m s^{-1})/(W m^{-2}).

$\Delta T_{\rm spot} = -550\,{\rm K}$ and $\Delta T_{\rm bright} = 46.5\,{\rm K}$, corresponding to the midpoints of the provided ranges.

Assuming the provided values of $\Delta T_{\rm spot}$ and $\Delta T_{\rm bright}$ and using the *SDO*/HMI-derived time series of $f_{\rm spot}$ and $f_{\rm bright}$, we fit Equation (1) to the SORCE/TIM TSI as shown in Figure 3. From this fit, we extract a quiet-Sun temperature ($T_{\rm quiet} = 5770.080 \pm 0.007$ K) and scaling coefficients ($a_{\rm bright} = 0.959 \pm 0.007$ and $a_{\rm spot} = 1.54 \pm 0.02$). These coefficients are consistent with the 20% and 50% definitional variations in feature area described in Meunier et al. (2010a).

The three-way agreement between the solar telescope $\log R'_{\rm HK}$, *SDO*/HMI filling factors, and SORCE/TIM TSI indicates that our activity models provide a consistent picture of solar magnetic processes. However, the solar telescope/HARPS-N solar RVs are not in full agreement with these activity measurements. In particular, Figure 1 shows that $\log R'_{\rm HK}$, $f_{\rm bright}$, and the TSI all display a downward trend over the 800 day observation period. The solar RVs do not display this trend. To quantify this disagreement, we compute the Spearman correlation coefficient between the solar RVs and $\log R'_{\rm HK}$, $f_{\rm bright}$, and TSI, yielding values of 0.42, 0.40, and 0.04, respectively. To understand this discrepancy, we now use *SDO*/HMI-derived RVs to reproduce solar telescope/HARPS-N measurements.

4. Calculating RV Contributions of Spots/Plage

We model the effects of stellar magnetic activity on RV measurements as a combination of two processes: the suppression of convection in magnetically active regions that leads to a net redshift of the spectrum ($\Delta \hat{v}_{\rm conv}$), and the effect of bright and dark active regions on the solar disk that leads to a photometric shift ($\Delta \hat{v}_{\rm phot}$). In the following sections, we discuss the physical origins of each term and their magnitudes as derived from *SDO*/HMI images. We then reconstruct the solar RVs from a combination of the two processes and fit this model to the RVs measured with the solar telescope/HARPS-N.

4.1. Suppression of Convective Blueshift, $\Delta \hat{v}_{conv}$

$\Delta \hat{v}_{\rm conv}$ results from the suppression of solar convective motions by local magnetic fields. Taking an intensity-weighted

average of the bright, upflowing plasma in the middle of the convective cells and dark, downflowing plasma at the cell edges results in an overall convective blueshift with an amplitude of approximately $250\,{\rm m\,s^{-1}}$ (Dravins et al. 1981; Meunier et al. 2010a). The plasma's interaction with solar magnetic fields impedes this convective motion and therefore attenuates this convective blueshift. Note that the convective blueshift of an observed spectral line depends on its formation depth in the photosphere (Gray 2009; Gray & Oostra 2018). The convective shift observed by *SDO*/HMI using the 6173.3 Å line will therefore differ from the solar telescope/HARPS-N observations, which are averaged over many lines. To account for this systematic difference, we apply a scaling coefficient in our RV reconstruction as discussed in Section 4.3.

In previous studies, Meunier et al. (2010b), Dumusque et al. (2014), and Haywood et al. (2016) found $\Delta \hat{v}_{\rm conv}$ to be the dominant source of RV shifts, with a disk-integrated amplitude of several $\rm m\,s^{-1}$. Using the *SDO*/HMI Dopplergrams in conjunction with the magnetic flux and continuum intensity images, we replicate the analysis of Haywood et al. (2016) to determine $\Delta \hat{v}_{\rm conv}$ for the full solar telescope/HARPS-N observing period. Several $\rm m\,s^{-1}$ variations are observed at the synodic rotation period of the Sun, along with long-term drifts of a similar amplitude as shown in the upper-left panel of Figure 4.

4.2. Photometric Shift, $\Delta \hat{v}_{phot}$

The presence of dark sunspots and bright plage on the solar disk break the Sun's symmetry about its rotation axis. This results in an imbalanced Doppler shift across the solar disk; it is this Doppler imbalance that results in $\Delta \hat{v}_{\rm phot}$, the photometric RV shift due to magnetic activity (Saar & Donahue 1997; Lagrange et al. 2010). As before, we use the methods of Haywood et al. (2016) to compute $\Delta \hat{v}_{\rm phot}$ using the *SDO*/HMI-measured full-disk magnetograms and continuum intensity. This time series is also shown in the lower-left panel of Figure 4 and, as expected, is significantly smaller than the shifts calculated for $\Delta \hat{v}_{\rm conv}$.

4.3. Reconstruction of Solar RVs from SDO/HMI Basis Functions

Following Haywood et al. (2016), we model the total solar telescope RVs, $\Delta {\rm RV}_{\rm model}$, using a linear combination of $\Delta \hat{v}_{\rm conv}$ and $\Delta \hat{v}_{\rm phot}$:

$$\Delta {\rm RV}_{\rm model} = A(t)\Delta \hat{v}_{\rm phot} + B(t)\Delta \hat{v}_{\rm conv} + {\rm RV}_0. \quad (2)$$

Here $A(t)$ and $B(t)$ are weighting coefficients for the photometric and convective RV shifts, and $\rm RV_0$ describes the zero-point of HARPS-N. As $\rm RV_0$ is a purely instrumental parameter, we expect it to remain constant with time. $A(t)$ and $B(t)$ describe the mapping of information from the single $\lambda = 6173.3$ Å spectral line onto the several thousand lines used in the HARPS-N CCF analysis (Baranne et al. 1996; Sosnowska et al. 2012). The coefficient $A(t)$ accounts for systematic differences between the bright and dark active regions observed with *SDO*/HMI and the spectrum observed with the solar telescope/HARPS-N, analogous to the scaling factors used in our TSI reconstruction (see Equation (1)). The coefficient $B(t)$ accounts for the systematic difference in the convective blueshift due to
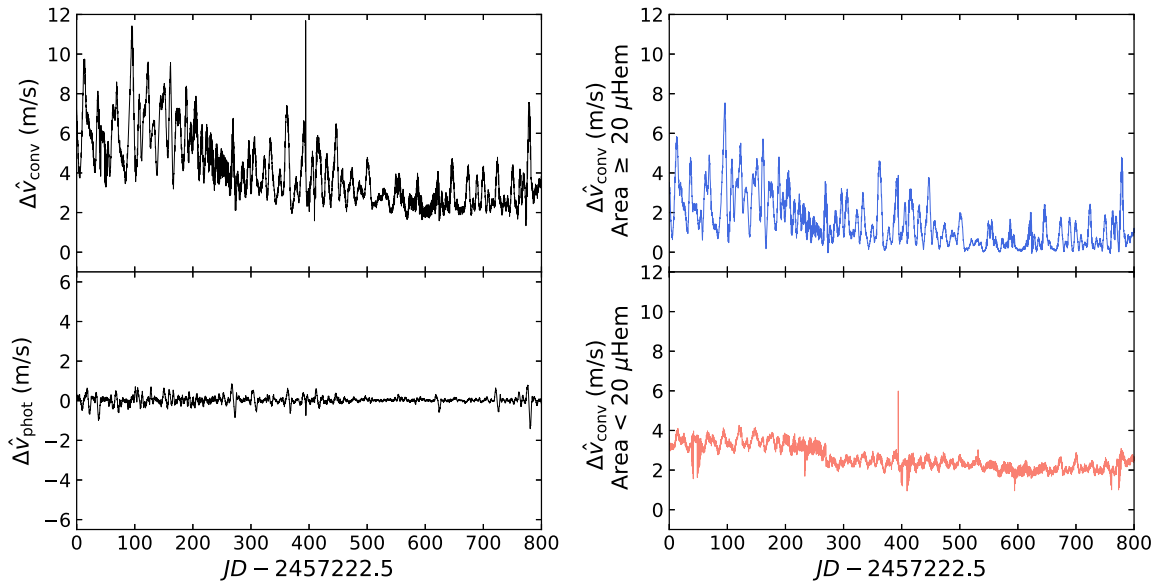
Figure 4. Left: *SDO*/HMI-derived estimates of the convective (top) and photometric velocities (bottom) using all active regions. Right: contributions of plage (area ⩾20 μHem, top) and network (area <20 μHem, bottom) to the suppression of convective blueshift. As in previous works (Meunier et al. 2010b; Haywood et al. 2016), we find that $\Delta\hat{v}_{\rm conv}$ dominates the effects of $\Delta\hat{v}_{\rm phot}$.

the different heights of formation of each spectral line. We thus expect $A(t)$ and $B(t)$ to be of order unity, but not necessarily equal to 1. In Haywood et al. (2016), $A(t)$, $B(t)$, and RV$_0$ are taken to be constant. However, these coefficients could vary with time perhaps due to additional magnetic processes at work, or some other changes over the activity cycle. We divide each time series into smaller subsections and calculate the fits for each subsection to investigate how $A(t)$ and $B(t)$ evolve in time.

As discussed in Section 2, we take daily averages of 2.5 yr of solar telescope data to mitigate the effects of solar p-modes and granulation. We expect that on timescales longer than several days, the measured RV variations are dominated by magnetic effects. We then fit Equation (2) to the whole data set, yielding global values of $A(t)$ and $B(t)$, as given in Table 2. Following Haywood et al. (2016), we include an uncorrelated noise parameter s, added in quadrature to the solar telescope/HARPS-N observational errors, to account for instrumental uncertainties and other processes not in our model (Collier Cameron et al. 2006).

We then divide the data into subsections of $N = 112$ days (corresponding to four synodic solar rotations per subsection) and repeat the fit, evaluating $A(t)$, $B(t)$, and RV$_0$ for each subsection. We chose this value of N to maximize the number of data sections while maintaining sufficiently small statistical uncertainties. The results described in the following sections do not depend on the exact value of N.

Since the RV contributions of magnetic active regions are modulated by the Sun's rotation (see Figures 4 and 6), we expect our model to fully capture RV variation on timescales of the rotation period (and its harmonics) and above. As shown in Figure 5, the dominant contributions to the observed RV variations occur on these timescales. Below the rotation period, the solar RV is modulated to some degree by magnetic region growth and decay, but also by granulation and supergranulation due to surface magneto-convection. Our model is not designed to capture these convective processes,

and we therefore do not expect it to capture all RV variations on these short timescales.

4.4. Active Region Area Dependence of Convective Shift

In addition to reconstructing the solar telescope/HARPS-N RVs variations, we investigate if and how the suppression of convective blueshift associated with a given active region depends on its size. Meunier et al. (2010a) speculated that small intergranular network features and large plage/sunspot regions would have different contributions to the convective blueshift, and Palumbo et al. (2017) observed different center-to-limb velocity variations for solar network and plage. We differentiate the RV contributions of these two classes of active region. The network and plage/spot regions may be distinguished based on their spatial distributions: while small network are uniformly distributed over the solar disk, large plage/spot regions appear only around active latitudes, leading to the well-known butterfly diagram (see Hathaway 2015 and references there-in).

To distinguish network from plage/spot regions, we plot the 2D distribution of active region co-latitude Θ and area, as shown in the left panel of Figure 6. There is a sharp cut at approximately 20 microhemispheres (i.e., 20 parts per million of the visible hemisphere), or $60\,{\rm Mm}^2$ in areal units. Active regions smaller than this cutoff are distributed across the Sun, while regions above the cutoff only appear around the equator, at $0.75 < \sin\Theta \leqslant 1$. We therefore use this area threshold to classify each active region as small network or large spot/plage.

To investigate the differing contributions of the network and spot/plage, we compute $\Delta\hat{v}_{\rm conv}$ as a function of time using only network and only spot/plage regions. From the resulting time series (see Figure 4) and periodograms (right panel of Figure 6), we observe that the majority of the RV variability at the solar rotation period is the result of large active regions: small regions do not significantly contribute to the suppression of convective blueshift on this timescale. Given these differing contributions, we perform the RV reconstruction of Section 4.3
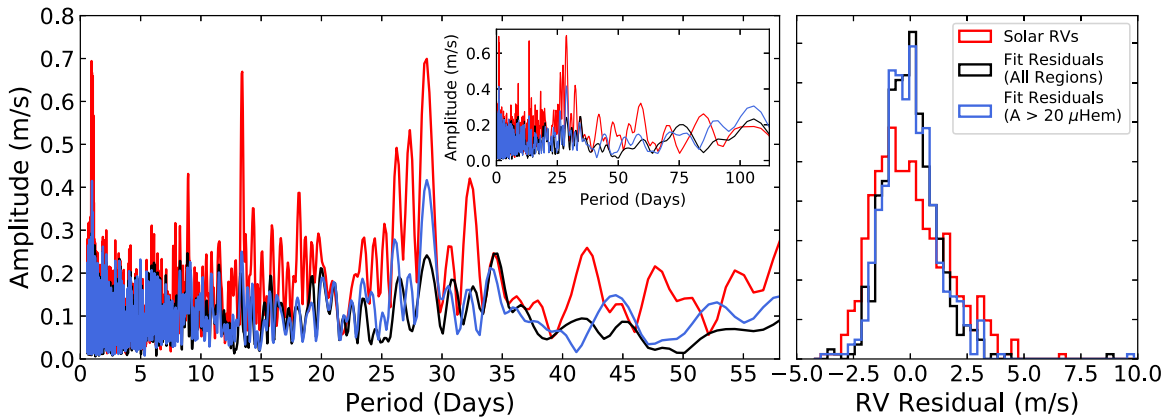
Figure 5. Left: periodogram of the solar telescope RVs (red), fit residuals using all active regions (black), and fit residuals using a 20 μHem area threshold (blue). We note that measured solar RVs have an amplitude of 0.72 m s^{-1} at the solar rotation period. Applying our model with no area cut reduces this amplitude to 0.24 m s^{-1}; including an area cut results in an amplitude of 0.42 m s^{-1}. *Inset:* a zoomed-out view of the periodogram. We note that the two fits successfully reduce the RV amplitudes observed on most timescales greater than the rotation period. Right: histogram of the RV residuals. Both fits result in Gaussian-distributed RV residuals: while both fits display decrease the rms RV residuals, applying an area threshold does not produce a visible change in the fit residuals. The area cut does, however, remove the unphysical trend in RV$_0$, as discussed in Section 5.2 and as shown in Figure 7.

first using the convective RV shift calculated using all observed active regions and second using the convective RV shift calculated using only large spots/plage. The results of this analysis are given in Figure 7 and Tables 1 and 2.

5. Discussion

5.1. Reconstruction of Solar RVs

As shown in Figure 7, both $A(t)$ and $B(t)$ are consistent with constant values, implying that $\Delta\hat{v}_{conv}$ and $\Delta\hat{v}_{phot}$ have a consistent effect on the solar telescope/HARPS-N measurements over the full observation period. The resulting $A(t)$ and $B(t)$ values are consistent with those reported by Haywood et al., as shown in Table 2. Haywood et al. (2016) measured the Sun close to solar maximum, observing a total magnetic filling factor $6\% < f_{total} < 10\%$, whereas near solar minimum, we observe $f_{total} < 5\%$. We also note that the rms amplitudes of $\Delta\hat{v}_{phot}$ and $\Delta\hat{v}_{conv}$ (shown in Table 1), calculated using network and plage regions, are consistent with or somewhat smaller than those of Meunier et al. (2010b) and Haywood et al. (2016), which is consistent with observations performed at different parts of the activity cycle. Given the agreement of our $A(t)$ and $B(t)$ values with those of Haywood et al. (2016), we may conclude that these parameters do not change significantly as the Sun enters activity minimum, and only weakly depend on the magnetic filling factor, if they do so at all.

Using only large plage/spot regions in our reconstruction of $\Delta\hat{v}_{conv}$ does not significantly change the magnitude of $A(t)$ and $B(t)$ compared to using all active regions. However, when all active regions are considered, the calculated instrumental offset $RV_0(t)$ (see Figure 7) slowly increases over the 3 year observation period. This slow increase disappears when our model assumes that only large active regions suppress the convective blueshift. We discuss the implications of this result in Section 5.2.

5.2. Long-timescale Variations: Changes in RV$_0$

As our model assumes that magnetic activity is fully described by $\Delta\hat{v}_{conv}$ and $\Delta\hat{v}_{phot}$, we expect RV$_0$ to be an instrument-dependent parameter related to the zero-point of HARPS-N, and therefore constant over our observation period.

HARPS-N exposures are calibrated using a simultaneous reference with sub-m s^{-1} precision (Cosentino et al. 2014), and the *SDO*/HMI basis functions are calculated relative to the quiet-Sun velocity (Haywood et al. 2016); long-term instrumental drifts are therefore calibrated out of each measurement and should not affect the value of RV$_0$.

However, in both fits to the solar telescope data, we find a systematic increase in RV$_0$. When all active regions are considered, we obtain a shift of $\Delta RV_0 = 2.6$ m s^{-1} over the course of the 800 day measurement period. Accounting for the area dependence of the convective velocity eliminates this variation almost entirely. This is consistent with our hypothesis regarding the area dependence of the convective velocity: small active regions do not meaningfully contribute to the suppression of convective blueshift on timescales of the solar rotation period. Instead, as shown in Figure 4 and the right panel of Figure 6, these small regions contribute a systematic drift on timescales of hundreds of days. Differentiating the contributions of small and large magnetic activity is therefore necessary for the successful detection of long-period, low-mass planets around solar-type stars.

Physically, this systematic RV shift may be due to the different contributions of plage and network, as demonstrated in Palumbo et al. (2017). Part of the active solar network results from decaying of plage regions, resulting in a correlation between the plage filling factor and the network RV contribution. This, in turn, may lead to an overall systematic RV shift. We may also consider a similar scenario for dark spots: small, dark solar pores lack penumbra, and therefore have a different contribution to the solar RV. As the Sun enters activity minimum, large spots become less common, leading to a larger relative pore contribution and therefore a systematic RV shift. In both cases, large and small active regions must therefore be treated separately in our RV reconstruction.

5.3. RV Residuals and Rotational Modulated Variations

The measured solar telescope/HARPS-N RV variations (Figure 1, top) have an rms scatter of 1.65 m s^{-1}. Subtracting the reconstructed values of ΔRV_{model} computed using all active regions and using the physically motivated constant value of RV$_0$ (assumed to be an instrumental offset) reduces
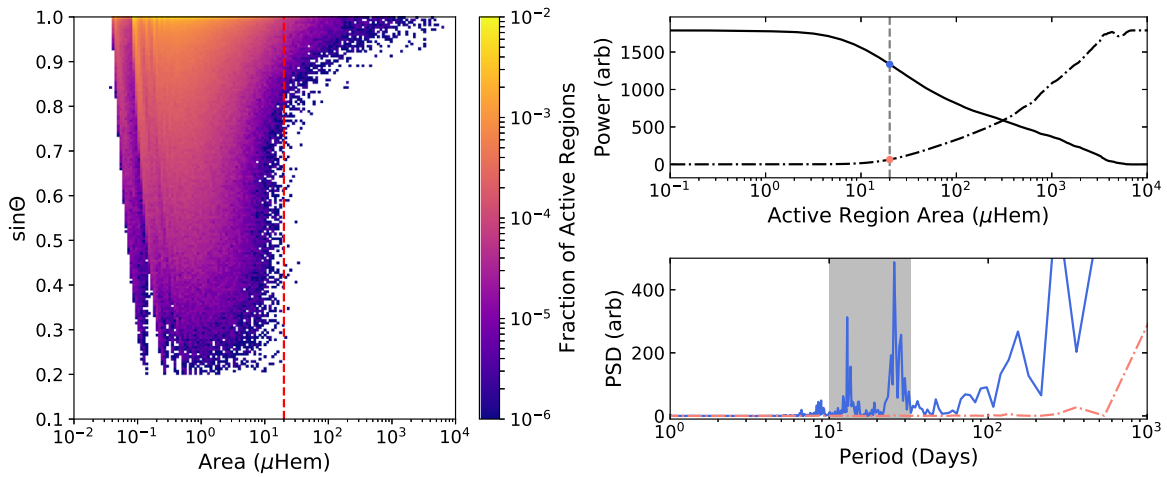
Figure 6. Left: fraction of observed solar active regions as a function of region area and co-latitude, Θ (as measured from the north pole). From the observed spatial distribution, we may divide the active regions into a small network, which appear all across the solar disk, and large spots/plage, which preferentially appear around activity latitudes. The sharp change in the spatial distribution allows us to infer the presence of a sharp cutoff allows us to infer an area threshold of 20 microhemispheres that separates these two regimes. Upper-right: power associated with the solar rotation period and its first harmonic above (solid) and below the area threshold (dashed). Power at these frequencies is evaluated by integrating the power spectral density (PSD) of the RV contributions for each region size over the shaded region, indicated below. Lower-right: PSD of RV contributions above (solid blue) and below (red dashed) microhemisphere. Below the 20 microhemisphere threshold, there is little power associated with the solar rotation period: these small structures therefore do not contribute to the solar RVs on the timescales of interest in this work.

this scatter to $1.31\,\mathrm{m\,s^{-1}}$. Repeating this analysis with an empirical time-varying value of $\mathrm{RV_0}$ reduces this scatter to $1.18\,\mathrm{m\,s^{-1}}$. Incorporating the area dependence of the convective shift into our model results in an rms scatter of $1.21\,\mathrm{m\,s^{-1}}$. While including this spatial information does not further improve the rms scatter of the RV residuals, it almost completely eliminates the observed change in $\mathrm{RV_0}$, and thus constitutes a more physically grounded and complete model, as previously discussed in Section 5.2.

As discussed at the end of Section 4.3 and as shown in Figure 6, we expect our model to eliminate the observed power at the solar rotation period. The measured solar telescope RV variations have an amplitude of $0.72 \pm 0.06\,\mathrm{m\,s^{-1}}$ at this timescale: applying our model using all active regions reduces this amplitude to $0.24 \pm 0.08\,\mathrm{m\,s^{-1}}$. Incorporating the area dependence of the convective shift into our model results in an amplitude of $0.42 \pm 0.08\,\mathrm{m\,s^{-1}}$ (see Figure 5). The residual signal at the rotation period may indicate that our area threshold does not perfectly differentiate plage and network regions: smaller plage regions are not being included in our calculated value of $\Delta\hat{v}_{\mathrm{conv}}$, resulting in an imperfect removal of the RV signal at the rotation period. Reducing the area threshold reduces the residual amplitude at the rotation period; however, the inclusion of network regions in the calculated $\Delta\hat{v}_{\mathrm{conv}}$ results in a non-zero trend in $\mathrm{RV_0}$. The residual signal may also result from the several-day lag between activity proxies and RV signals observed by Dumusque et al. (2014) and Collier Cameron et al. (2019). Lastly, we note that our model assumes the network regions have the same RV contribution as the quiet Sun: in reality, however, we expect network to provide an additional, nontrivial RV contribution Palumbo et al. (2017). A more sophisticated model will be required to fully describe these network-driven variations.

In summary, the reconstructed RVs leave over $1\,\mathrm{m\,s^{-1}}$ of RV variations unaccounted for: these may be the result of supergranulation, which has a physical timescale longer than the 6–8 hr solar observation period at the TNG (Del Moro et al. 2004;

Meunier et al. 2015). They may also result from additional surface velocity flows unaccounted for in our model, RV differences of network relative to quiet Sun, or an unaccounted for instrumental systematic.[20]

5.4. Magnetic Activity Indicators and Active Region Area

The agreement between the magnetic filling factors, R'_{HK}, and TSI demonstrated in Section 3 confirms that the traditional metrics for solar activity are all self-consistent. However, the correspondence between these activity indicators is not improved by separately considering large and small active regions: the chromospheric emission captured by $\log R'_{\mathrm{HK}}$ is strongly correlated with the total magnetic filling factor, not the large region filling factor. Similarly, the TSI may only be accurately reproduced using both large and small active regions. All the magnetic active regions on the Sun have an enhanced chromospheric column density that strengthens the emission reversals in the Ca II H&K line cores, and all bright/dark regions will modulate the Sun's overall brightness. These traditional stellar activity indicators are thus correlated only with the overall coverage of active features, and not the size of each feature. Given the observed dependence of the suppression of convective blueshift on active region size, we may therefore conclude new activity indicators correlated with active region sizes are needed to successfully reproduce RV variations on distant stars.

6. Conclusions

In this work, we analyze 3 yr of solar observations during the decline of Carrington Cycle 24 to test models of radial-velocity variations of Sun-like stars. We compare solar telescope/

---

[20] The HARPS/HARPS-N DRS was recently upgraded to improve the stability of the daily wavelength calibrations. At the time of writing, the HARPS-N solar data had not yet been reprocessed with the new DRS. We understand that the older version of the software has an uncertainty of up to $1\,\mathrm{m\,s^{-1}}$ in the RV zero points between successive days of observation.
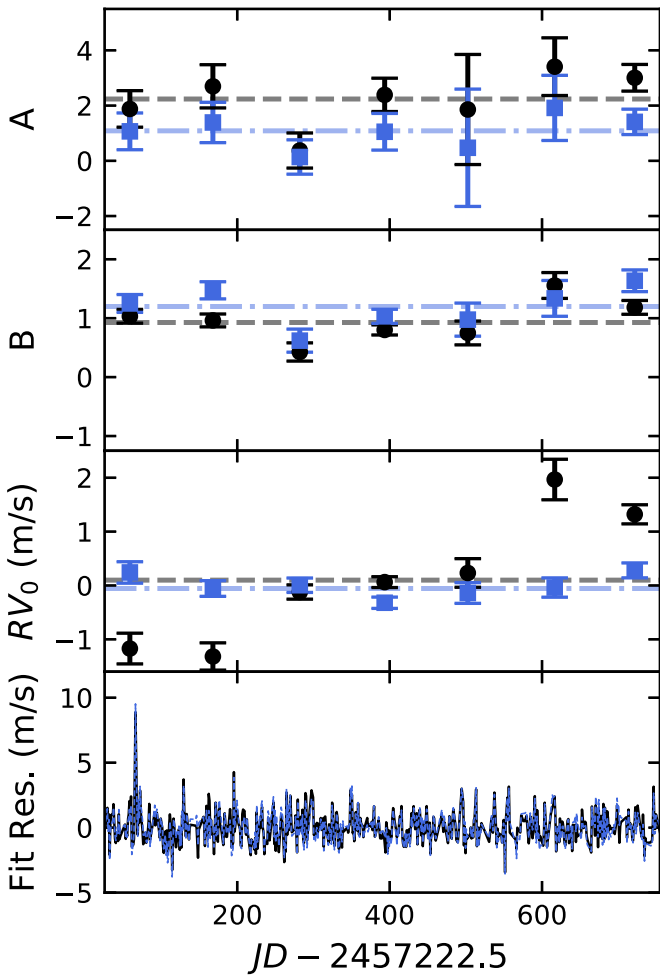
Figure 7. First and second panel: fit parameters $A(t)$, $B(t)$, for the unitless scaling parameters for the photometric and convective RV shifts, $\Delta\hat{v}_{phot}$, and $\Delta\hat{v}_{conv}$ derived from *SDO*/HMI (plotted in Figure 4). Third panel: RV offset $(RV_0(t))$ in m s^{-1}. Parameters fitted to HARPS-N solar RVs using Equation (2) (see the text) in $N = 112$ day sets, using all active regions (black points) or a 20 μHem area threshold (blue squares). Statistical error bars are plotted for each parameter. Fourth panel: residuals of both fits.

Table 1
rms Amplitudes of RV Time Series

Basis Function	All Active Regions	Area $\geqslant 20\mu$Hem	Haywood et al. (2016)	Meunier et al. (2010b)
$\Delta\hat{v}_{phot}$	0.21 m s^{-1}	0.21 m s^{-1}	0.17 m s^{-1}	0.42 m s^{-1}
$\Delta\hat{v}_{conv}$	1.69 m s^{-1}	0.88 m s^{-1}	1.30 m s^{-1}	1.39 m s^{-1}
HARPS-N RV	1.64 m s^{-1}			

Note. We include the time series derived using all regions (left column of Figure 4) and using only plage regions (right column of Figure 4). As a point of comparison, we also include the values of Haywood et al. (2016; also derived from *SDO*/HMI), the values of Meunier et al. (2010b; derived from the Michelson Doppler imager onboard the *Solar and Heliospheric Observatory*), and the solar telescope measurements of the solar RVs (top panel of Figure 1).

HARPS-N measurements of the solar RVs and $\log R'_{HK}$, *SDO*/HMI disk-resolved activity images, and SORCE/TIM measurements of the TSI. As expected, the observed values of

$\log R'_{HK}$ and TSI are strongly correlated with the overall magnetic filling factor derived from *SDO*/HMI images.

However, these activity indicators are not straightforward predictors of the observed solar RV variations. While we see a slow decrease in $\log R'_{HK}$, TSI, and magnetic filling factor as the Sun enters cycle minimum, we do not observe this decrease in the solar telescope/HARPS-N RV variations. To investigate this discrepancy, we model the solar RV as a linear combination of the suppression of convective blueshift and rotational flux imbalance. Our initial reconstruction of the solar RV variations decreased the rms scatter from 1.65 to 1.18 m s^{-1} and reduced the RV amplitude at the rotation period by a factor of four, but only by introducing an arbitrary systematic drift of 2.6 m s^{-1} over the 800 day observation period. By computing contribution of each active region to the suppression of convective blueshift, we find that active regions smaller than 20 ppm (60 Mm^2) do not significantly suppress the convective blueshift. Including this area dependence in our model does not further decrease the overall rms scatter, and results in a factor of two reduction of the RV amplitude at the rotation period. However, it completely eliminates the need to introduce an arbitrary systematic drift in our reconstructed RVs, resulting in a more physically grounded model. We propose two possible causes for this drift: small changes in the network coverage that affect our quiet-Sun reference velocity due to RV differences between network and the quiet Sun Palumbo et al. (2017) or RV differences between spots (with penumbrae) and pores (without penumbrae), which are modulated by the changing spot filling factor. In either scenario, more detailed studies of the RV contributions of large and small scale features will be required to elucidate the mechanisms involved.

The different contributions of plage and network to the activity-driven RV variations explain why the calcium H/K activity index does not systematically correlate strongly with RV variations in Sun-like stars on timescales comparable to the magnetic cycle. On highly active stars, where large plage regions dramatically outnumber the small network regions, the plage filling factor will be approximately equivalent to the overall filling factor. We therefore expect the traditional activity indicators, such as $\log R'_{HK}$ and optical light curves, to provide a useful proxy for activity-driven RV variations in this regime. On low-activity stars, where the plage and network filling factors are comparable, separating the contributions of plage and network will be necessary to reproduce activity-driven RV variations. As the traditional activity indicators are correlated with the overall filling factor, they will not provide as useful a proxy of the activity-driven RV variations. For exoplanet RV surveys to be successful for low-activity stars, we must therefore identify correlates for activity region size.

The residuals of our fit still have an rms spread of over 1.21 m s^{-1}. This additional scatter may be the result of some long-term granulation process Meunier (2018), additional surface velocity flows, additional magnetic effects of network Palumbo et al. (2017), or unaccounted for systematic variation in the spectrograph on timescales shorter than the solar rotational period. Determining the physical origin of these residual RV variations, identifying correlates for active region size, and verifying that the observed relationships between RV and active region size hold as the Sun enters the active phase of the magnetic cycle will be the subject of future investigations.

Table 2
Average RV Fit Parameters

Parameter	Basis Function	All Active Regions	Area $\geqslant 20\mu$ Hem	Haywood et al. (2016)
$A(t)$	$\Delta\hat{v}_{\mathrm{phot}}$	2.24 ± 0.60	1.09 ± 0.58	2.45 ± 2.02
$B(t)$	$\Delta\hat{v}_{\mathrm{conv}}$	0.93 ± 0.11	1.20 ± 0.15	1.85 ± 0.27
RV_0		102.51 ± 0.06 m s^{-1}	102.36 ± 0.13 m s^{-1}	99.80 ± 0.28 m s^{-1}
s		1.21 m s^{-1}	1.23 m s^{-1}	2.70 m s^{-1}

Note. We compute the SDO/HMI-derived ΔRV_{model} by fitting to the solar telescope/HARPS-N RVs using Equation (2); the resulting time-averaged fit values are given above. We provide values derived using both network and plage regions, replicating the analysis of Haywood et al. (2016), as well as values derived using only the plage regions (see the text). The time variation of these parameters is shown in Figure 7. We also include the results of Haywood et al. (2016) as a point of comparison. Error bars on each parameter are statistical uncertainties and s is the added white noise beyond the 40 cm s^{-1} noise associated with each solar telescope observation.

Appendix A
Calculation of *SDO*/HMI-derived Quantities

In this work, we compute the filling factors of sunspots and plage and the radial velocities (RVs) associated with the suppression of convective blueshift and rotational imbalance. These calculations are based on the methods of Haywood et al. (2016), with some differences. Here we briefly review the methods of that paper, highlighting the differences in our implementation.

A.1. Identifying Active Regions

We identify solar active regions using the same thresholding methods as Haywood et al. (2016). We identify active regions using the line-of-sight HMI magnetograms. Active pixels have a magnetic field greater than

$$|B| > 3\sigma/\mu,$$

where $\sigma = 8$ G, the shot noise per SDO/HMI pixel, and $\mu = \cos\theta$, where θ gives the angular position from the center of the Sun.

To differentiate between dark spots and bright plage, we apply an intensity threshold. We compute the average quiet-Sun intensity I_{quiet} by averaging all the inactive pixels identified using the above threshold. Pixels are identified as spots using the intensity threshold of Yeo et al. (2013)—that is, if

$$I_{ij} < 0.89 * I_{,\mathrm{quiet}}.$$

The overall, spot, and plage filling factors are calculated simply by computing the fraction of SDO/HMI pixels corresponding to a given active region type relative to the number of pixels on the solar disk, N_{Sun}:

$$f_{\mathrm{total}} = \frac{1}{N_{\mathrm{sun}}} \sum_{ij} W_{ij}.$$

Here $W_{ij} = 1$ if pixel-ij corresponds to an active region and is 0 otherwise. The same equation may be used to calculate the bright (plage/network) and spot filling factors, f_{bright} and f_{spot}: in those cases, $W_{ij} = 1$ if pixel-ij corresponds to falls above or below the intensity threshold described previously. We therefore find that $f_{\mathrm{total}} = f_{\mathrm{bright}} + f_{\mathrm{spot}}$.

Table 3
Daily-averaged Solar Measures

JD—2457222.5	RV	σ_{RV}	$\log R'_{\mathrm{HK}}$	$f_{\mathrm{spot}} \times 10^3$	$f_{\mathrm{bright}} \times 10^3$	$\Delta\hat{v}_{\mathrm{phot}}$	$\Delta\hat{v}_{\mathrm{conv}}$	$\Delta\hat{v}_{\mathrm{conv,small}}$	$\Delta\hat{v}_{\mathrm{conv,large}}$
1.405	102.922	0.402	−4.973	0.182	34.169	0.168	5.803	2.732	3.237
10.438	104.131	0.4	−4.967	0.303	42.539	−0.307	7.949	4.203	3.441
10.947	104.602	0.4	−4.965	0.271	43.784	−0.214	8.386	4.596	3.577
11.968	104.754	0.401	−4.963	0.386	45.955	−0.002	9.135	5.402	3.73
12.965	105.195	0.401	−4.965	0.356	46.37	0.093	9.407	5.679	3.819
14.035	105.606	0.397	−4.963	0.264	44.349	0.175	9.084	5.412	3.847
14.975	105.808	0.393	−4.962	0.246	44.673	0.289	8.23	4.611	3.911
15.571	105.224	0.39	−4.961	0.299	45.293	0.299	7.575	4.027	3.842
17.042	103.588	0.399	−4.958	0.595	44.351	0.424	6.473	3.242	3.657
17.512	104.507	0.39	−4.957	0.756	43.556	0.492	6.238	3.111	3.631
19.468	103.439	0.4	−4.97	1.277	41.337	0.246	6.611	3.348	3.463
19.716	103.975	0.402	−4.971	1.316	41.01	0.133	6.68	3.337	3.448
22.471	100.788	0.4	−4.978	1.136	39.226	−0.554	6.757	2.66	3.507
22.504	101.162	0.4	−4.978	1.129	39.216	−0.553	6.746	2.649	3.51
29.425	103.184	0.516	−4.986	0.046	29.373	0.111	4.574	1.476	3.214
30.006	102.178	0.45	−4.98	0.049	29.155	0.083	4.378	1.314	3.145
31.351	101.838	0.404	−4.972	0.227	30.244	0.017	4.137	1.107	3.066
32.267	99.889	0.404	−4.979	0.461	31.03	0.15	4.124	1.186	3.064
33.261	102.153	0.399	−4.976	0.697	32.619	0.313	4.705	1.956	3.076
33.751	103.12	0.393	−4.973	0.845	33.721	0.341	5.182	2.501	3.031
34.579	104.932	0.4	−4.97	1.064	34.662	0.238	6.219	3.361	3.101
37.195	105.65	0.403	−4.961	1.66	39.151	−0.798	8.446	4.431	3.256
38.04	104.555	0.402	−4.967	1.595	40.119	−0.899	7.969	3.904	3.162
38.994	102.762	0.406	−4.971	1.465	42.171	−0.722	7.135	3.09	3.324
40.011	101.493	0.408	−4.971	1.231	44.358	−0.363	6.17	2.417	3.4
40.953	101.741	0.403	−4.97	0.436	41.352	0.017	5.607	2.281	3.342
41.938	102.048	0.406	−4.968	0.051	37.677	0.039	5.978	2.329	3.688
42.896	102.305	0.408	−4.976	0.05	38.559	0.037	5.814	2.229	3.625
43.918	102.659	0.403	−4.976	0.069	38.382	0.09	5.732	2.249	3.574
44.981	103.054	0.406	−4.973	0.103	36.822	0.106	5.632	2.247	3.49
⋮	⋮	⋮	⋮	⋮	⋮	⋮	⋮	⋮	⋮

Note. We provide the daily-averaged values of the Solar Telescope/HARPS-N and *SDO*/HMI measured velocities and activity indicators used in our analysis. Please see the Appendix B for a full description of the data.

(This table is available in its entirety in machine-readable form.)

A.2. Calculation of Active Region Velocities

A.2.1. The Convective Velocity, $\Delta\hat{v}_{conv}$

Our calculation of the activity-driven RV shifts differs slightly from that of Haywood et al. (2016). Our calculation of $\Delta\hat{v}_{conv}$ is given by computing the disk-averaged Doppler velocity, $\hat{v}$, and subtracting the disk-averaged quiet-Sun velocity, $\hat{v}_{\mathrm{quiet}}$:

$$\Delta\hat{v}_{\mathrm{conv}} = \hat{v} - \hat{v}_{\mathrm{quiet}}$$

$\hat{v}$ is the intensity-weighted average of the Dopplergram, with the spacecraft velocity and rotation profile ($\hat{v}_{\mathrm{sc}}$ and $\hat{v}_{\mathrm{rot}}$) removed,

$$\hat{v} = \frac{\sum_{ij}(v_{ij} - v_{\mathrm{sc},ij} - v_{\mathrm{rot},ij})I_{ij}}{\sum_{ij}I_{ij}},$$

and $\hat{v}_{\mathrm{quiet}}$ is the intensity-weighted average over the quiet pixels only:

$$\hat{v}_{\mathrm{quiet}} = \frac{\sum_{ij}(v_{ij} - v_{\mathrm{sc},ij} - v_{\mathrm{rot},ij})I_{ij}\bar{W}_{ij}}{\sum_{ij}I_{ij}\bar{W}_{ij}},$$

where $\bar{W}_{ij} = 1$ for inactive pixels and is 0 otherwise.

A.2.2. The Photometric Velocity, $\Delta\hat{v}_{phot}$

The photometric velocity is calculated as

$$\hat{v}_{\mathrm{phot}} = \frac{\sum_{ij}v_{\mathrm{rot},ij}(I_{ij} - \hat{K}L_{ij})W_{ij}}{\sum_{ij}I_{ij}}.$$

Here $\hat{K}$ is the average quiet-Sun intensity at disk center and L_{ij} gives the limb darkening at the ijth pixel.

Appendix B
Data

In Table 3, we provide the daily averaged solar telescope and *SDO*/HMI data products used in our analysis. We include the Julian date of each observation the solar telescope RV and associated uncertainty, the solar telescope measured $\log R'_{\mathrm{HK}}$ value, the HMI-derived spot and bright region filling factors, and the HMI-derived photometric and convective velocity shifts. All velocities have units of $\mathrm{m\,s^{-1}}$. $\Delta\hat{v}_{\mathrm{con,small}}$ and $\Delta\hat{v}_{\mathrm{con,large}}$ refer to the convective velocity shifts due to active regions with area <20 ppm and area ⩾20 ppm, respectively. Only the first 30 days of observations are listed here: the full table is available in machine readable format.

ORCID iDs

T. W. Milbourne https://orcid.org/0000-0001-5446-7712
R. D. Haywood https://orcid.org/0000-0001-9140-3574
D. F. Phillips https://orcid.org/0000-0001-5132-1339
H. M. Cegla https://orcid.org/0000-0001-8934-7315
A. C. Cameron https://orcid.org/0000-0002-8863-7828
X. Dumusque https://orcid.org/0000-0002-9332-2011
D. W. Latham https://orcid.org/0000-0001-9911-7388
J. Maldonado https://orcid.org/0000-0002-2218-5689
L. Malavolta https://orcid.org/0000-0002-6492-2085
A. Mortier https://orcid.org/0000-0001-7254-4363
F. Bouchy https://orcid.org/0000-0002-7613-393X
N. Buchschacher https://orcid.org/0000-0002-3697-1541
D. Charbonneau https://orcid.org/0000-0002-9003-484X
A. Ghedina https://orcid.org/0000-0003-4702-5152
A. G. Glenday https://orcid.org/0000-0002-5656-4396
M. Lodi https://orcid.org/0000-0002-5432-9659
M. López-Morales https://orcid.org/0000-0003-3204-8183
G. Micela https://orcid.org/0000-0002-9900-4751
E. Molinari https://orcid.org/0000-0002-1742-7735
G. Piotto https://orcid.org/0000-0002-9937-6387
K. Rice https://orcid.org/0000-0002-6379-9185
D. Sasselov https://orcid.org/0000-0001-7014-1771
A. Sozzetti https://orcid.org/0000-0002-7504-365X
A. Szentgyorgyi https://orcid.org/0000-0002-0255-2525

References

Auvergne, M., Bodin, P., Boisnard, L., et al. 2009, A&A, 506, 411
Baranne, A., Queloz, D., Mayor, M., et al. 1996, A&AS, 119, 373
Borucki, W. J., Koch, D., Basri, G., et al. 2010, Sci, 327, 977
Broomhall, A.-M., Chaplin, W. J., Davies, G. R., et al. 2009, MNRAS, 396, L100
Collier Cameron, A., Mortier, A., Phillips, D., Dumusque, X., et al. 2019, MNRAS, submitted
Collier Cameron, A., Pollacco, D., Street, R. A., et al. 2006, MNRAS, 373, 799
Cosentino, R., Lovis, C., Pepe, F., et al. 2012, Proc. SPIE, 8446, 8446
Cosentino, R., Lovis, C., Pepe, F., et al. 2014, Proc. SPIE, 9147, 9147
Couvidat, S., Schou, J., Hoeksema, J. T., et al. 2016, SoPh, 291, 1887
Del Moro, D. 2004, A&A, 428, 1007
Del Moro, D., Berrilli, F., Duvall, T. L., Jr., & Kosovichev, A. G. 2004, SoPh, 221, 23
Dravins, D., Lindegren, L., & Nordlund, A. 1981, A&A, 96, 345
Dumusque, X., Boisse, I., & Santos, N. C. 2014, ApJ, 796, 132
Dumusque, X., Glenday, A., Phillips, D. F., et al. 2015, ApJL, 814, L21
Dumusque, X., Udry, S., Lovis, C., Santos, N. C., & Monteiro, M. J. P. F. G. 2011, A&A, 525, A140
Fischer, D. A., Anglada-Escude, G., Arriagada, P., et al. 2016, PASP, 128, 066001
Fligge, M., Solanki, S. K., & Unruh, Y. C. 2000, A&A, 353, 380
Giorgini, J. D., Yeomans, D. K., Chamberlin, A. B., et al. 1996, BAAS, 28, 1158
Gray, D. F. 2009, ApJ, 697, 1032
Gray, D. F., & Oostra, B. 2018, ApJ, 852, 42
Harvey, J., Hill, F., Kennedy, J., Leibacher, J., & Livingston, W. 1988, AdSpR, 8, 117
Hathaway, D. H. 2015, LRSP, 12, 4
Haywood, R. D., Collier Cameron, A., Unruh, Y. C., et al. 2016, MNRAS, 457, 3637
Hoeksema, J. T., Baldner, C. S., Bush, R. I., Schou, J., & Scherrer, P. H. 2018, SoPh, 293, 45
Howell, S. B., Sobeck, C., Haas, M., et al. 2014, PASP, 126, 398
Isaacson, H., & Fischer, D. 2010, ApJ, 725, 875
Kjeldsen, H., Bedding, T. R., Butler, R. P., et al. 2005, ApJ, 635, 1281
Kopp, G., Heuerman, K., & Lawrence, G. 2005, SoPh, 230, 111
Kopp, G., & Lawrence, G. 2005, SoPh, 230, 91
Lagrange, A.-M., Desort, M., & Meunier, N. 2010, A&A, 512, A38
Linsky, J. L., & Avrett, E. H. 1970, PASP, 82, 169
Löhner-Böttcher, J., & Schlichenmaier, R. 2013, A&A, 551, A105
Mayor, M., & Queloz, D. 1995, Natur, 378, 335
Meunier, N. 2018, A&A, 615, A87
Meunier, N., Desort, M., & Lagrange, A.-M. 2010a, A&A, 512, 39
Meunier, N., Lagrange, A.-M., Borgniet, S., & Rieutord, M. 2015, A&A, 583, A118
Meunier, N., Lagrange, A.-M., & Desort, M. 2010b, A&A, 519, A66
Noyes, R. W., Hartmann, L. W., Baliunas, S. L., Duncan, D. K., & Vaughan, A. H. 1984, ApJ, 279, 763
Palle, P. L., Jimenez, A., Perez Hernandez, F., et al. 1995, ApJ, 441, 952
Palumbo, M. L., Haywood, R. D., Saar, S. H., et al. 2017, AGUFM, P53B-2651
Pepe, F. A., Cristiani, S., Lopez, R. R., et al. 2010, Proc. SPIE, 7735, 7735
Pesnell, W. D., Thompson, B. J., & Chamberlin, P. C. 2012, SoPh, 275, 3
Phillips, D. F., Glenday, A. G., Dumusque, X., et al. 2016, Proc. SPIE, 9912, 9912
Reiners, A., Lemke, U., Bauer, F., Beeck, B., & Huke, P. 2016, A&A, 595, A26
Ricker, G. R., Winn, J. N., Vanderspek, R., et al. 2014, JATIS, 1, 1
Rottman, G. 2005, SoPh, 230, 7
Saar, S. H., & Donahue, R. A. 1997, ApJ, 485, 319
Schou, J., Scherrer, P. H., Bush, R. I., et al. 2012, SoPh, 275, 229
Schrijver, C. J., & Zwaan, C. 2000, Solar and Stellar Magnetic Activity (Cambridge: Cambridge Univ. Press)
Shapiro, A. I., Solanki, S. K., Krivova, N. A., et al. 2014, A&A, 569, A38
Sosnowska, D., Lodi, M., Gao, X., et al. 2012, Proc. SPIE, 8451, 8451
Vaughan, A., Preston, G., & Wilson, O. 1978, PASP, 90, 267
Wilson 1968, ApJ, 153, 221
Yeo, K. L., Solanki, S. K., & Krivova, N. A. 2013, A&A, 550, A95
Zeng, L., & Sasselov, D. 2013, PASP, 125, 227